Chemical Engineering Journal 150 (2009) 561–568

Contents lists available at ScienceDirect

Chemical Engineering Journal

journal homepage: www.elsevier.com/locate/cej

In-flight thermal treatment of soda-lime-silica glass powders for glass production by argon–oxygen induction thermal plasmas

M. Mofazzal Hossain[a], Yaochun Yao[b], Takayuki Watanabe[c,*], Fuji Funabiki[d], Tetsuji Yano[d]

[a] Department of Electronics and Communications Engineering, East West University, 43 Mohakhali, Dhaka 1212, Bangladesh
[b] Kunming University of Science & Technology, Kunming 650093, Yunnan Province, China
[c] Department of Environmental Chemistry and Engineering, Tokyo Institute of Technology, G1-22, 4259 Nagatsuta, Yokohama 226-8502, Japan
[d] Department of Chemistry and Materials Science, Tokyo Institute of Technology, S7-4, 2-12-1 O-okayama, Tokyo 152-8550, Japan

ARTICLE INFO

Article history:
Received 21 October 2008
Received in revised form 28 February 2009
Accepted 2 March 2009

Keywords:
Soda-lime-silica
Heat transfer
Powder
Simulation
Porosity
Particle trajectory

ABSTRACT

In order to investigate the plasma–particle energy exchange dynamics and optimize the plasma discharge and particle parameters during in-flight thermal treatment of soda-lime-silica glass powders, a plasma–particle interaction model was developed. This model solved the conservation equations to predict the plasma temperature and flow fields, and then calculated the injected individual particle trajectories and temperature histories, and the particle source terms to take into account the plasma–particle interaction. It was noticed that particle injection significantly reduced the plasma temperature around the centerline of the torch and hence decreased the heat transfer to particles at higher carrier gas flow-rate and powder feed-rate. As a result the size and composition of quenched particles were affected significantly by the above factors. The simulated results were consistent with those of experiment, which provided valuable guidelines in optimizing the plasma discharge and particle parameters for the efficient thermal treatment of soda-lime-silica glass particles.

1. Introduction

Induction thermal plasmas (ITP) have extensively been used for the synthesis and surface treatment of fine powders since couple of decades as a clean reactive heat source [1,2]. ITP technology may ensure essentially the in-flight one-step melting, short melting time, and less pollution compared with the traditional technologies that have been using in the glass industries for the vitrification of raw glass powders [3]. The partially vitrified glass powders may be used in glass production. Moreover, powers having high porosity may be vitrified to reduce their porosity or solidify the powders. During in-flight treatment of particles, it is rare to have experimental records of thermal history of particles; only some diagnosis of the quenched particles is possible for the characterization. Thus, the numerical analysis is the only tool to have comprehensive characterization of the particle thermal history and energy exchange during in-flight treatment. Our aim is to determine the in-flight thermal treatment mechanism of soda-lime-silica glass powders by ITP and to optimize the plasma discharge parameters, particle size and feed-rate of input powders that affect the quenched powders size, morphology, and compositions. The thermal treatment of injected particles depends mainly on the plasma–particle heat transfer efficiency, which in turn depends to a large extent on the trajectory and temperature history of the injected particles. Thus, for numerical investigation it is the challenge to predict the trajectory and temperature history of the particles injected into the ITP torch. Among others Yoshida et al. [4] pioneered the modeling of particle heating in induction plasmas; though their work assumed the particle trajectory along the centerline of the torch only. Boulos [5] developed a model and comprehensively discussed the thermal treatment of alumina powders in the fire ball of argon induction plasma. Later Proulx et al. [6] predicted the trajectory and temperature history of alumina and copper particles injected into ITP torch and discussed the particle loading effects in argon induction plasma. To achieve our goal, a plasma–particle interaction model has been developed for argon–oxygen plasma, including a nozzle inserted into the torch for the injection of carrier gas and soda-lime-silica glass powders. This model can be used to demonstrate the particle loading effects and to optimize the parameters that govern the particles trajectory, temperature history, quenched particles size and plasma–particle energy exchange efficiency for any plasma gas combination.

2. Modeling

2.1. Plasma model

The photograph of the plasma torch is presented in Fig. 1 and the schematic geometry and dimensions of the ITP torch is

* Corresponding author. Tel.: +81 45 924 5414; fax: +81 45 924 5414.
E-mail address: watanabe@chemenv.titech.ac.jp (T. Watanabe).

1385-8947/$ – see front matter © 2009 Elsevier B.V. All rights reserved.
doi:10.1016/j.cej.2009.03.013

Nomenclature

A_c	complex amplitude of vector potential
B	magnetic field vector
C_D	drag coefficient
C_p	specific heat at constant pressure
C_{pp}	particle specific heat at constant pressure
D_a	ambipolar diffusion coefficient
d_p	particle diameter
D_{ion}	Diffusion coefficient of ion
D_{ij}	binary diffusion coefficient between species i and j
D^m	multicomponent diffusion coefficient
E	electric field vector
g	acceleration of gravity
h	enthalpy
h_c	heat transfer coefficient
H_m	latent heat of melting
H_v	latent heat of vaporization
i	complex vector ($\sqrt{-1}$)
J	current density vector
Kn	Knudsen number
M_i	molecular weight of species i
M_j	molecular weight of species of j
N_t^0	total number of particles injected per unit time
n_d	particle size distribution
n_r	fraction of N_t^0 injected at each point
Nu	Nusselt number
p	pressure
Pr	Prandtl number
Q	net heat exchange between the particle and its surroundings
Q_{net}	net energy transferred to all the particles injected per unit time
Q_r	volumetric radiation loss
Q_t	net energy transferred to a particle throughout the trajectory
Re	Reynold number
S_p^C	particle source term in continuity equation
S_p^M	particle source term in momentum equation
S_p^E	particle source term in energy equation
t	time
T	plasma temperature
T_a	ambient temperature
T_b	boiling point temperature of particles
T_e	electron temperature
T_h	heavy particle temperature
T_{ion}	ion temperature
T_p	particle temperature
t_s	residence time of particle in the plasma
u	velocity vector
u_p	axial velocity component of particle
U_R	relative speed of particles with respect to plasma
v_p	radial velocity component of particle
x_i	mole fraction of species i
y	mass fraction

Greek symbols

∇	vector operator
κ	thermal conductivity
ρ	mass density
μ	viscosity
σ	electrical conductivity
μ_0	permeability of free space
ω	angular frequency ($2\pi f$)
$\overline{\Omega}_{ij}^{(1.1)}$	collision integral between species i and j
ε	particle porosity
σ_s	Stefan–Boltzmann constant
χ	liquid mass fraction of a particle
$\propto$	thermal accommodation coefficient
γ	specific heat ratio

Subscripts

f	properties corresponding to film temperature
p	particle
s	properties corresponding to particle temperature
∞	properties corresponding to plasma temperature
(i, j)	location of a control volume or cell

Superscripts

(l, k)	particles having an initial diameter d_l, and injection point r_k

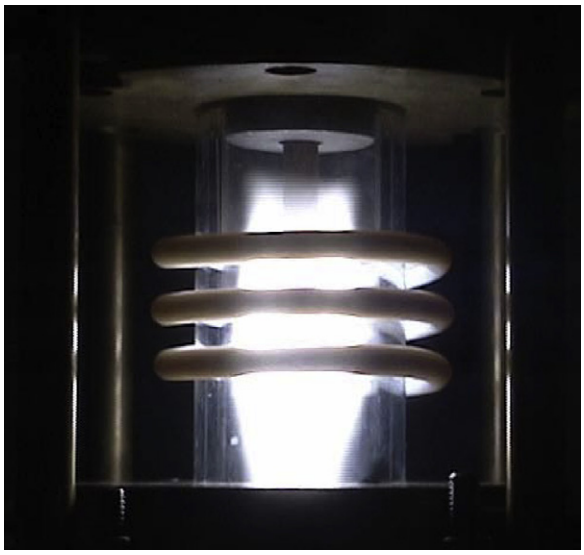

Fig. 1. A photograph of induction plasma torch.

presented in Fig. 2. The torch dimensions and discharge conditions are tabulated in Table 1. The overall coupling efficiency of the reactor, i.e. the ratio of plasma power to plate power supply is assumed to be 50%. In our experiment, the plate power was 20 kW

Table 1
Torch dimensions and discharge conditions.

Distance to initial coil position (L_1)	19 mm
Length of injection tube (L_t)	52 mm
Distance to end of coil position (L_2)	65 mm
Torch length (L_3)	190 mm
Coil diameter (d_c)	5 mm
Wall thickness of quartz tube (T_{wall})	1.5 mm
Inner radius of injection tube (r_1)	1 mm
Outer radius of injection tube (r_t)	4.5 mm
Outer radius of inner slot (r_2)	6.5 mm
Inner radius of outer slot (r_3)	21.5 mm
Torch radius (r_0)	22.5 mm
Coil radius (r_c)	32 mm
Plasma power	10 kW
Working frequency	4 MHz
Working pressure	0.1 MPa
Flow rate of carrier gas (Q_1)	4–9 lpm of argon
Flow rate of plasma gas (Q_2)	2 lpm of argon
Flow rate of sheath gas (Q_3)	22 lpm argon and 2 lpm oxygen

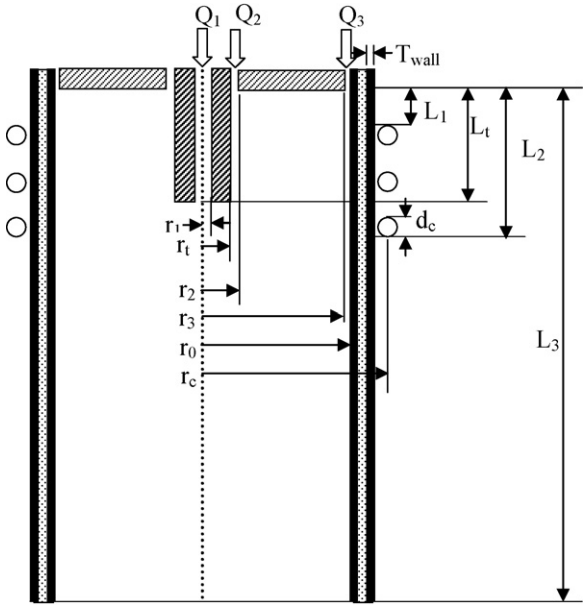

Fig. 2. Schematic geometry and dimensions of induction thermal plasma torch.

so assuming 50% overall coupling efficiency, the plasma power was put to 10 kW. This assumption is quite reasonable according to the literature of induction thermal plasma torch. The model solves the conservation equations and vector potential form of Maxwell's equations simultaneously under LTE (local thermodynamic equilibrium) conditions, including a metal nozzle inserted into the torch. It is assumed that plasma flow is two-dimensional, axi-symmetric, laminar, steady, optically thin, and electromagnetic fields are two-dimensional [7]. Adding the source terms to the conservation equations, the plasma–particle interaction and particle loading effects have been taken into account. In this model, the conservation equations are as follows:

Mass conservation:

$$\nabla \cdot \rho \mathbf{u} = S_p^C \tag{1}$$

Momentum conservation:

$$\rho \mathbf{u} \cdot \nabla \mathbf{u} = -\nabla p + \nabla \cdot \mu \nabla \mathbf{u} + \mathbf{J} \times \mathbf{B} + S_p^M \tag{2}$$

Energy conservation:

$$\rho \mathbf{u} \cdot \nabla h = \nabla \cdot \left(\frac{\kappa}{C_p} \nabla h \right) + \mathbf{J} \cdot \mathbf{E} - Q_r - S_p^E \tag{3}$$

Species conservation:

$$\rho \mathbf{u} \cdot \nabla y = \nabla \cdot (\rho D^m \nabla y) + S_p^C \tag{4}$$

Vector potential form of Maxwell electromagnetic field equation [8]:

$$\nabla^2 A_c = i \mu_0 \sigma \omega A_c \tag{5}$$

2.1.1. Boundary conditions

The boundary conditions for the mass, momentum, energy and species conservation equations are: at the inlet, gas temperature was set to 300 K and uniform velocity profiles are assumed based on the given flow rates; on the axis of symmetry, the symmetry conditions are imposed; on the walls, no-slip condition is assumed; the outer wall temperature is set to 350 K; and, at the exit, axial gradients of all fields are set equal to zero. The inserted nozzle is assumed to be water cooled at 300 K. On the nozzle wall, the velocity is set to zero. The boundary conditions for the vector potential form of Maxwell's equation are the same as those described in Ref. [8].

2.1.2. Computational procedure and thermophysical properties

The conservation equations, which are listed in previous section, are solved numerically using the SIMPLER algorithm of Patankar [9]. The algorithm is based on a control-volume finite-difference scheme for solving the transport equations of incompressible fluids. Calculations are performed for a 44 (in radial direction) by 93 (in axial direction) non-uniform grid system.

Thermodynamic and transport properties of argon and oxygen gases required for the simulation are mass density, specific heat at constant pressure, viscosity, electrical and thermal conductivity and radiative loss coefficient. The transport properties, which are function of temperature, are calculated under LTE conditions using Chapman-Enskog first approximation to Boltzmann equation [10]. The effective diffusion coefficient of species is calculated based on the following equations:

$$D_i^m = \frac{1 - y_i}{\sum_{j \neq i, j=1}^{\upsilon} x_i / D_{ij}} \tag{6}$$

$$D_{ij} = 2.628 \times 10^{-2} \sqrt{\frac{M_i + M_j}{2 M_i M_j}} \frac{T^{1.5}}{\Omega_{ij}^{(1.1)}} \tag{7}$$

The ambipolar diffusion coefficient for ions can be approximated as $D_a = D_{ion}(1 + T_e/T_{ion})$. As the thermal equilibrium condition, i.e. $T_h = T_e = T_{ion}$ was applied thus, $D_a \cong 2D_{ion}$.

2.2. Particle model

The following assumptions are made in the analysis of plasma–particle interactions in the ITP torch; the particle motion is two-dimensional, only the viscous drag force and gravity affect the motion of an injected particle, the temperature gradient inside the particle is neglected, and the particle charging effect caused by the impacts of electrons or positive ions is negligible. Because the size of the particles considered in the simulation is very large compared with the atomic or molecular size of the powders. The particle charging effects have not been intensively studied yet. However, the electromagnetic drag forces caused by the particle charging of the injected particles are negligible compared with those by neutrals and charged particles due to negligible electrical conductivity of soda-lime-silica powders. Thus, the momentum equations for a single spherical particle injected vertically downward into the plasma torch can be expressed as follows:

$$\frac{du_p}{dt} = -\frac{3}{4} C_D (u_p - u) U_R \left(\frac{\rho}{\rho_p d_p} \right) + g \tag{8}$$

$$\frac{dv_p}{dt} = -\frac{3}{4} C_D (v_p - v) U_R \left(\frac{\rho}{\rho_p d_p} \right) \tag{9}$$

$$U_R = \sqrt{(u_p - u)^2 + (v_p - v)^2} \tag{10}$$

The particle temperature, liquid fraction and diameter are predicted according to the following energy balances:

$$Q = \pi d_p^2 h_c (T - T_p) - \pi d_p^2 \sigma_s \varepsilon (T_p^4 - T_a^4) \tag{11}$$

$$\frac{dT_p}{dt} = \frac{6Q}{\pi \rho_p d_p^3 C_{pp}} \quad \text{for } T_p < T_b \tag{12}$$

$$\frac{d\chi}{dt} = \frac{6Q}{\pi \rho_p d_p^3 H_m} \quad \text{for } 1000 \leq T_p \leq 1600 \tag{13}$$

$$\frac{dd_p}{dt} = -\frac{2Q}{\pi \rho_p d_p^2 H_v} \quad \text{for } 1000 \leq T_p \leq 1600,\ T_p \geq T_b \tag{14}$$

Drag coefficient C_{Df} is calculated using Eq. (15) and the property variation at the particle surface layer and the non-continuum effects are taken into account by Eqs. (16) and (17) [11].

$$C_{Df} = \begin{cases} \dfrac{24}{R_e} & R_e \le 0.2 \\ \dfrac{24}{R_e}\left(1+\dfrac{3}{16}R_e\right) & 0.2 < R_e \le 2.0 \\ \dfrac{24}{R_e}(1+0.11{R_e}^{0.81}) & 2.0 < R_e \le 21.0 \\ \dfrac{24}{R_e}(1+0.189R_e^{0.62}) & 21.0 < R_e \le 200 \end{cases} \quad (15)$$

$$f_1 = \left(\frac{\rho_\infty \mu_\infty}{\rho_s \mu_s}\right)^{-0.45} \quad (16)$$

$$f_2 = \left\{1+\left(\frac{2-\alpha}{\alpha}\right)\left(\frac{\gamma}{1+\gamma}\right)\frac{4}{Pr_s}Kn\right\}^{-0.45}, \quad 10^{-2} < Kn < 0.1 \quad (17)$$

$$C_D = C_{Df} f_1 f_2 \quad (18)$$

To take into account the steep temperature gradient between plasma and particle surface, the Nusselt correlation can be expressed by Eq. (19) [12]. The non-continuum effect is taken into account by Eq. (20) [11].

$$Nu_f = (2.0 + 0.6R_{ef}^{1/2}Pr_f^{1/3})\left(\frac{\rho_\infty \mu_\infty}{\rho_s \mu_s}\right)^{0.6}\left(\frac{C_{p\infty}}{C_{ps}}\right)^{0.38} \quad (19)$$

$$f_3 = \left\{1+\left(\frac{2-\alpha}{\alpha}\right)\left(\frac{\gamma}{1+\gamma}\right)\frac{4}{Pr_s}Kn\right\}^{-1}, \quad 10^{-3} < Kn < 0.1 \quad (20)$$

The convective heat transfer coefficient is predicted as follows:

$$h_c = \frac{\kappa_f}{d_p} Nu_f f_3 \quad (21)$$

2.2.1. Particle source terms

Let us assume N_t^0 be the total number of particles injected per unit time, n_d is the particle size distribution, and n_r is the fraction of N_t^0 injected at each point through the injection nozzle. Thus, the total number of particles per unit time traveling along the trajectory (l, k) corresponding to a particle diameter d_l injected at the inlet point r_k is:

$$N^{(l,k)} = n_{d_l} n_{r_k} N_t^0 \quad (22)$$

For the sake of computation, the particle concentration n_r in the inlet is assumed to be uniform and to be separated into five injection points, which are at radial positions of 0.3, 0.45, 0.6, 0.75 and 0.9 mm. In the present computation the particles diameter distribution is assumed to be Maxwellian (similar to experiment). The particle size and corresponding distribution fraction are presented in Table 2. In the present computation, the powder is assumed to be composed of seven size particles according to its diameter and deviation. The average particle diameter is 58 μm and the maximum deviation is 67%. As a result, there are 35 different possible trajectories of the injected particles. The injection velocity of the particles is assumed to be equal to the injection velocity of carrier gas.

To take into account the particles loading effects, particles source terms for the mass, momentum, energy and species conservation equations have been calculated in the same fashion as described in Ref. [6], using the Particle-Source-In Cell (PSI-CELL) approach [13], where the particles are regarded as sources of mass, momentum and energy. The source terms in the mass and species conservation equation, S_p^C is the net efflux rate of particles mass in a computational cell (control volume). Assuming the particles are spherical, the efflux rate of particle mass for the particle trajectory (l, k) that traverses a given cell (i, j) is:

$$S_{p,ij}^{C(l,k)} = \frac{1}{6}\pi\rho_p N_{ij}^{(l,k)}(d_{ij,in}^3 - d_{ij,out}^3) \quad (23)$$

The net efflux rate of particle mass is obtained by summing over all particles trajectories which traverse a given cell (i, j):

$$S_{p,ij}^C = \sum_l \sum_k S_{p,ij}^{C(l,k)} \quad (24)$$

The source terms for momentum conservation equations are evaluated in the same fashion as that of mass conservation equation. In this case, the efflux rate of particles momentum for the particle trajectory (l, k) traversing a given cell (i, j) is:

$$S_{p,ij}^{M_z(l,k)} = \frac{1}{6}\pi\rho_p N_{ij}^{(l,k)}(u_{ij,in}d_{ij,in}^3 - u_{ij,out}d_{ij,out}^3) \quad (25)$$

$$S_{p,ij}^{M_r(l,k)} = \frac{1}{6}\pi\rho_p N_{ij}^{(l,k)}(v_{ij,in}d_{ij,in}^3 - v_{ij,out}d_{ij,out}^3) \quad (26)$$

Thus, the corresponding source terms for axial and radial momentum conservation equations are:

$$S_{p,ij}^{M_z} = \sum_l \sum_k S_{p,ij}^{M_z(l,k)} \quad (27)$$

$$S_{p,ij}^{M_r} = \sum_l \sum_k S_{p,ij}^{M_r(l,k)} \quad (28)$$

The source term for energy conservation equation $S_{p,ij}^E$ consists of the heat given to the particles $Q_{p,ij}^{(l,k)}$, and superheat to bring the particle vapors into thermal equilibrium with the plasma $Q_{v,ij}^{(l,k)}$:

$$Q_{p,ij}^{(l,k)} = \int_{\tau_{in}}^{\tau_{out}} \pi d_p^2 h_c (T_{ij} - T_{p,ij}^{(l,k)})\, dt \quad (29)$$

$$Q_{v,ij}^{(l,k)} = \int_{\tau_{in}}^{\tau_{out}} \frac{\pi}{2}\pi d_p^2 \rho_p \left(\frac{dd_p}{dt}\right) C_{pv}(T_{ij} - T_{p,ij}^{(l,k)})\, dt \quad (30)$$

$$S_{p,ij}^E = \sum_l \sum_k N_{ij}^{(l,k)}(Q_{p,ij}^{(l,k)} + Q_{v,ij}^{(l,k)}) \quad (31)$$

The calculation is started by solving the plasma temperature and flow fields without injection of any particles. Using these conversed temperature and flow fields, particles trajectories together with particle temperature and size histories are calculated. The particle source terms for the mass, momentum and energy conservation equations for each control volume throughout the torch are then predicted. The plasma temperature and flow fields are predicted again incorporating these particle source terms. The new plasma temperature and flow fields are used to recalculate the particles trajectories, temperature and size histories. Calculating the new source terms and incorporating them into conservation equations constitute the effects of plasma–particle interaction, thereby completing the cycle of mutual interaction. The above computation schemes are repeated until convergence. The physical properties of soda-lime-silica glass powders used in the present investigation are listed in Table 3.

Table 2
Particle size and corresponding distribution fraction.

Particle diameter (μm)	20	40	50	68	77	80	90
Fraction	0.03	0.07	0.1	0.6	0.1	0.07	0.03

3. Simulated results

The calculation has been carrier out for a plasma power of 10 kW, reactor pressure 0.1 MPa and induction frequency 4 MHz. The discharge conditions are tabulated in Table 1. In this study, attention

Table 3
Physical properties of soda-lime-silica glass powders.

Mass density	2300 kg/m^3
Specific heat at constant pressure	800 J/kg K
Porosity	80%
Fusion temperature	1000–1600 K
Boiling temperature	2500 K
Latent heat of fusion	3.69×10^5 J/kg
Latent heat of vaporization	1.248×10^7 J/kg

is given to the plasma–particle interaction effects on individual particle trajectory, velocity, and temperature history along the trajectories for different carrier gas flow-rate and powder feed-rates. Attention also paid to investigate how the plasma–particle energy exchange process is affected by the particle loading effects. Two aspects of the thermal treatment are investigated: the behavior of the individual particles, and the global effects of the particles on the plasma fields. The carrier gas flow-rate is very vital in determining the individual particle trajectories, and the allowable powder feed-rate. Fig. 3 shows the isotherms in the torch for a carrier gas flow-rate of 6 lpm argon and various powder feed-rates. The other discharge conditions are the same as presented in Table 1. A comparison among the isotherms clearly reveals the intense cooling around the torch centerline that increases with powder feed-rate. However, the plasma temperature away from the centerline of the torch remains almost unaffected by higher powder feed-rates. This is because the individual particle trajectories are not widely outbound in the radial direction; rather the trajectories are very close to the torch axis. Thus, the plasma–particle interaction around the centerline is very crucial at higher powder feed-rate. The same kind of arguments is proposed by Ye et al. [14] to explain the particle trajectories for alumina and tungsten particles. The effects of carrier gas flow-rates on the individual particle trajectories are presented in Fig. 4, for the particle diameter of 50 μm and a feed-rate of 5 g/min. It is comprehended that the higher flow-rate of carrier gas enhances the axial velocity of the particles, because the initial axial velocity of the particles depends on carrier gas flow rate; as a result the trajectories become closer to the torch axis at higher flow-rate. The individual particle temperature history along the trajectory is also influenced by the carrier gas flow-rate and powder feed-rate. Fig. 5 shows the effects of carrier gas flow-rate on the particle temperature for a feed-rate of 5 g/min. It is found that the particle temperature along the trajectory decreases at higher carrier gas flow-rate. The main reason is the cooling of plasma at higher carrier gas flow-rate that leads less heat transfer to particles. As the particle's boiling or vaporization temperature is 2500 K, particle temperature cannot be greater than the boiling point temperature. In Fig. 5, for a carrier gas flow-rate of 4 lpm, the curve is flat with axial distance along the torch length (from 142 mm to 190 mm) because, particles attain the boiling point temperature earlier than those for higher carrier gas flow-rate.

Fig. 6 describes the effects of powder feed-rate on the particle temperature along the trajectory. Like the flow-rate of carrier gas, the higher feed-rate of powder also causes intense cooling of

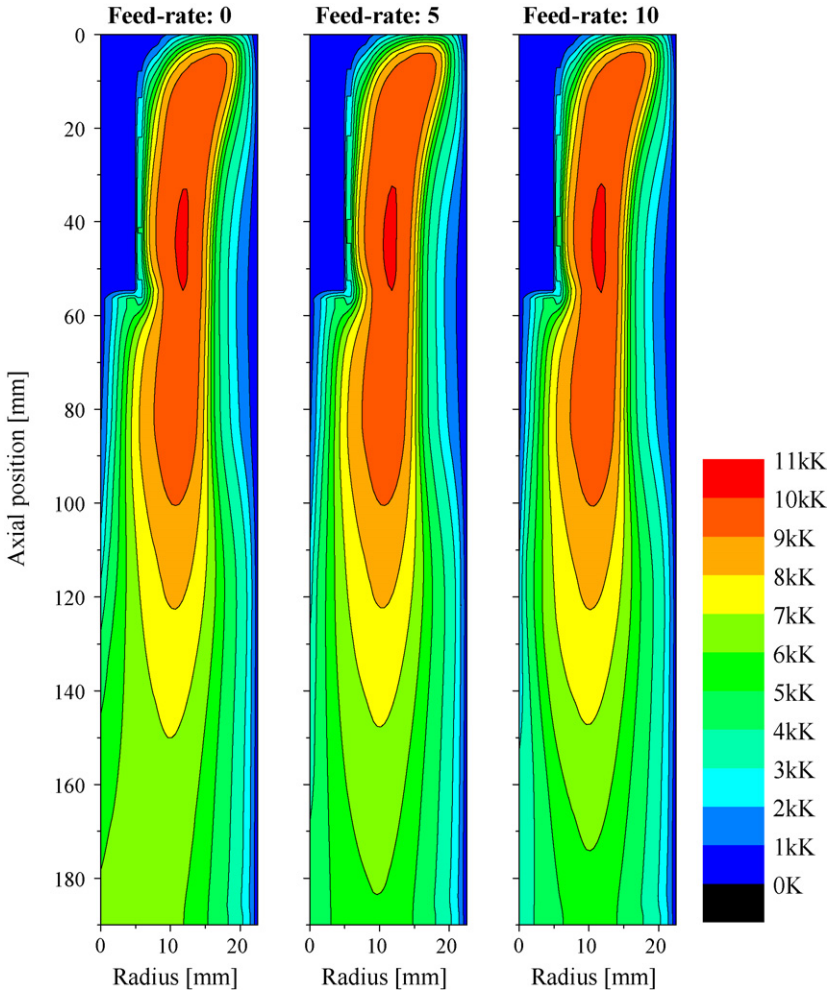

Fig. 3. Effects of powder loading on the isotherms for a carrier gas flow-rate of 6 lpm.

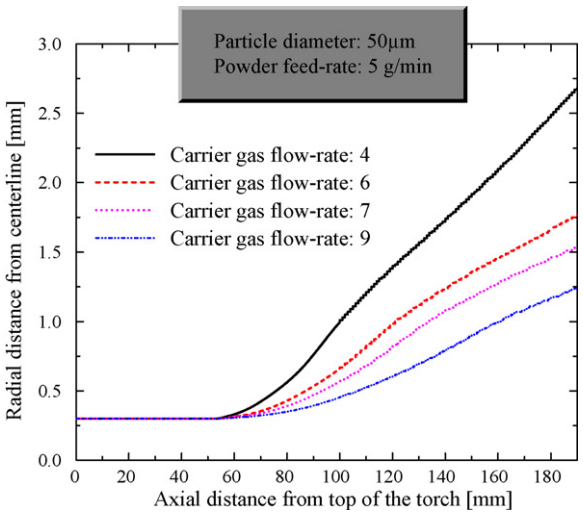

Fig. 4. Effects of carrier gas flow-rate on the particle trajectories for a powder feed-rate of 5 g/min.

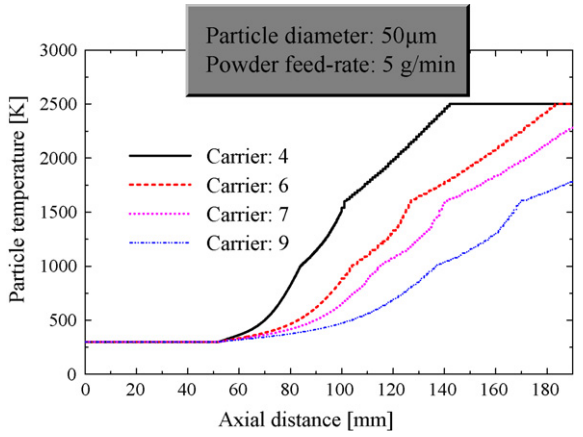

Fig. 5. Dependence of particle temperature history along the trajectory on carrier gas flow-rate.

plasma; thus, the heat transfer to particles decreases what results lower particle temperature. At this stage of investigation, it is indeed necessary to discuss the energy transfer mechanism to particles. The energy transfer is affected by the particles physical properties, plasma temperature, and velocity. The last two parameters are affected to a large extent by the carrier gas flow-rate and powder

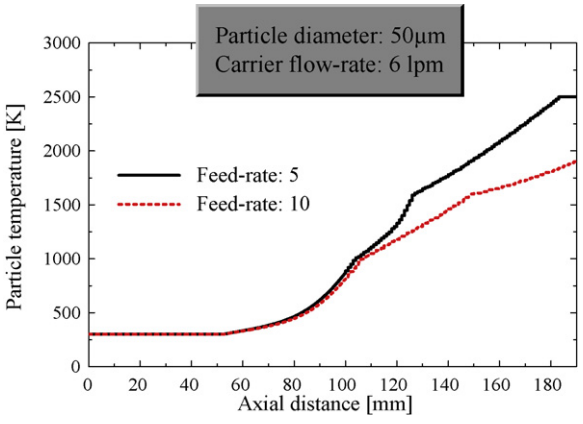

Fig. 6. Dependence of particle temperature history along the trajectory on the powder feed-rate.

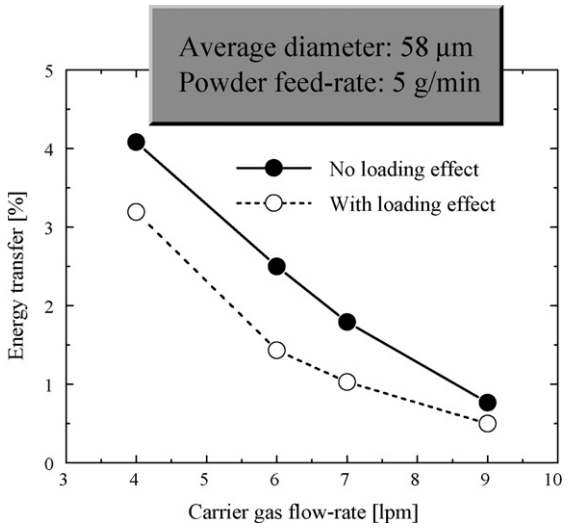

Fig. 7. Effects of powder loading and carrier gas flow-rate on the plasma–particle energy transfer.

loading. The net energy transfer to particles is calculated by integrating the energy transfer rate to the particles injected per unit time over the residence time for all the particle trajectories. Mathematically the net energy transfer to particles (Q_{net}) can be expressed as follows:

$$Q_t = \int_{t=0}^{t=t_s} \{\pi d_p^2 h_c(T - T_p) - \pi d_p^2 \sigma_s \varepsilon (T_p^4 - T_a^4)\}\, dt \tag{32}$$

$$Q_{net} = \sum_l \sum_k N^{(l,k)} Q_t \tag{33}$$

Fig. 7 clearly presents how the net energy transfer to particles is affected by the carrier gas flow-rate under powder loading conditions. Only 5 g/min of powder feeding decreases the energy transfer to particle by about 44%. The powder loading effect and the dependence of energy transfer to particles on the powder feed-rate is presented in Fig. 8, for a carrier gas flow-rate of 9 lpm. It can be noticed that energy transfer to particles increases linearly with feed-rate in the absence of particle loading effect; however, when particle loading effect is taken into account, energy transfer to particles still increases with the feed-rate but with a declined slop. With the increase of powder feed-rate the total energy transfer increases

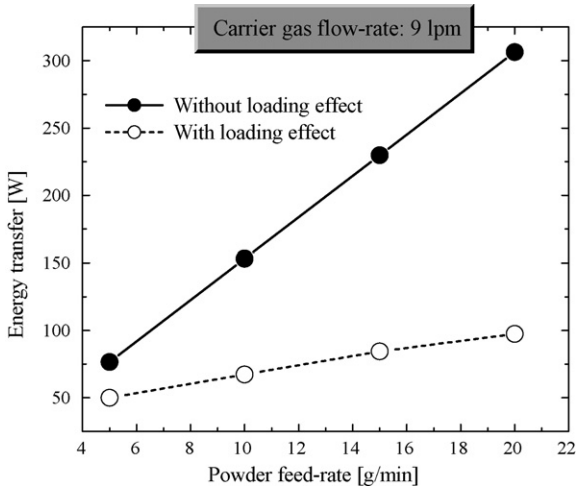

Fig. 8. Particle loading effects on plasma–particle energy transfer at various powder feed-rate.

but the energy transfer per unit mass of powder actually decreases when powder loading effect is taken into account (broken line of Fig. 8). This fact is clearly evident from the broken line of Fig. 8, when powder loading effect is taken into account, which situation is very close to the experimental condition. The main reason is the intense local cooling of plasma around the torch centerline under dense particle loading. It is also evident that the particle loading effect is pronounced at higher powder feed-rate.

4. Experimental

4.1. Setup

The experimental setup consists of a plasma torch (Fig. 1), a reaction chamber, powder feeder, and a power supply unit (4 MHz, 20 kW). The plasma torch consists of a water-cooled co-axial quartz tube surrounded by a three-turn induction coil. The soda-lime-silica glass powders are prepared by spray-drying method from the reagents of Na_2CO_3, $CaCO_3$ and SiO_2 with the composition of Na_2O:16, CaO:10 and SiO_2:74 in wt%. The mean diameter and porosity of soda-lime-silica glass powders are 58 μm and 80%, respectively. The plasma discharge conditions are the same as those described in Table 1 in the modeling section. The soda-lime-silica glass powders are injected into ITP torch along with the carrier gas at a rate of 5–20 g/min and the quenched powders are collected on a water-cooled ceramic block at 340 mm from the nozzle exit.

4.2. Characterization of plasma-treated particles

The treatment quality of the powders is characterized by the vitrification degree, the surface morphology, cross-sectional structure and composition of the quenched powders. The vitrification degree is defined as the ratio of the converted crystalline phases of SiO_2 in the quenched powder to the crystalline SiO_2 in the raw powders. The vitrification degree of quenched powders is quantitatively determined by X-ray diffractometry (XRD) on Miniflex (Rigaku) with Cu Kα radiation at 30 kV and 15 mA. The data are collected in the 2θ range 3–90° with a step size of 0.02° and a scan speed of 4°/min. The quenched powders collected at the reaction chamber are examined by scanning electron microscopy (SEM) on JSM5310 (JEOL) to observe their surface morphologies and cross-sectional microstructures. The composition of quenched powders is analyzed by inductively coupled plasma (ICP) on ICP-8100 (SHIMADZU).

4.3. Experimental results

In the experiment soda-lime-silica glass powders are injected along with the carrier gas through the nozzle inserted into the plasma torch. Thus, the initial particle velocity is the same as that of carrier gas. When the particles come in contact to high temperature plasma flame, they are heated and their temperature starts to rise. As the particle temperature reaches to its melting temperature, particle porosity decreases drastically; as a result, particle diameter shrinks. When particle temperature reaches to its boiling temperature, vaporization takes place and particle diameter shrinks further. In order to investigate the effects of carrier gas flow-rate and powder feed-rate on energy transfer to particles, the vitrification degree and Na_2O evaporation rate are estimated through XRD and ICP spectrum analysis. Higher vitrification degree and Na_2O evaporation rate indirectly indicate the large energy transfer to particles. Fig. 9 shows the XRD and ICP spectrum analysis results. It can be noticed that both the evaporation rate of Na_2O and the vitrification degree decrease with the increase of both carrier gas flow-rate [Fig. 9(a)] and powder feed-rate [Fig. 9(b)]. The vitrification degree and the

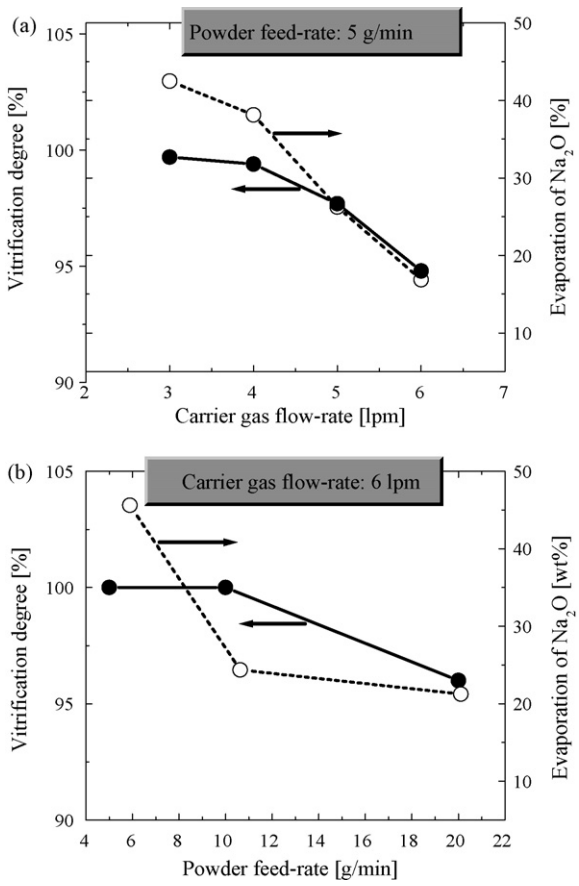

Fig. 9. Effects of carrier gas flow-rate (a), and powder feed-rate (b) on the vitrification degree and Na_2O evaporation rate.

evaporation of Na_2O depend to a large extent on the particle temperature. Higher carrier gas flow-rate and powder feed-rate cause lower plasma temperature which causes less heat transfer to particles; as a result particle temperature is lower. It is important to underline that after the thermal treatment, the size, composition, and morphology of the particles have been changed significantly. The effects of thermal treatment are visualized in the SEM photograph as shown in Fig. 10. From Fig. 10(a) and (b), it can be noticed that after treatment, the particle size becomes smaller, quite spherical, smoother and compact surface.

5. Discussions

To validate our modeling and simulated results, a comparative discussion between simulated and experimental results are indeed necessary. From the experimental results it is found that at higher carrier gas flow-rate and powder feed-rate, both the evaporation rate of Na_2O and the vitrification degree decrease. These results indicate that less heat transfer to particles takes place at higher carrier gas flow-rate and powder feed-rate. From the simulated results it is evident that at increased carrier gas flow-rate and powder feed-rate, the energy transfer to particles decreases; as a result, particles temperature becomes lower. It is convinced that the main reason of less heat transfer to particles is the severe local cooling of plasma around the torch centerline at higher carrier gas flow-rate and powder feed-rate. Thus, it may be argued that the simulated results well agree with the experimental findings.

From experimental results, high vitrification degree of raw material is always accompanied by high evaporation of Na_2O. The high evaporation loss of Na_2O indicates the change of glass com-

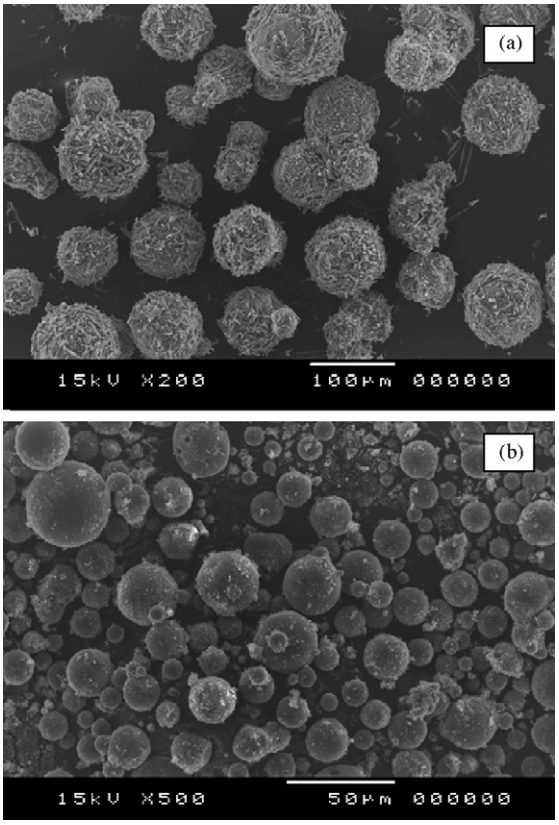

Fig. 10. The SEM photographs of soda-lime-silica glass powders before (a), and after (b) thermal treatment.

position and the increase of cost. Hence, it is necessary to find an optimized condition to obtain a high vitrification degree with lower Na_2O evaporation under the direction of this model.

6. Conclusions

A plasma–particle interactive flow model has been developed to simulate the particle trajectories, temperature histories. The developed model can be used to optimize the carrier gas flow-rate, particle size, and powder feed-rate to achieve the maximum treatment efficiency during thermal treatment of soda-lime-silica glass powders by argon–oxygen induction thermal plasmas. Numerically, it is found that the heat transfer to particles decreases at increased carrier gas flow-rate and powder feed-rate, and these results well agree with those of experiment. Thus, it can be concluded that, efficient thermal treatment of particles depends not only on the physical properties of the particles, but also on the plasma discharge conditions and particle parameters. Therefore, for a particular type of powder (certain physical properties) both carrier gas flow-rate and powder feed-rate mainly govern the treatment quality.

Acknowledgements

This work was partially supported by JSPS (Japan Society for the Promotion of Science), and the Energy Innovation Program of NEDO (New Energy and Industrial Technology Development Organization), Japan.

References

[1] X. Fan, T. Ishigaki, Y. Sato, Phase formation in molybdenum disilicide powders during in-flight induction plasma treatment, J. Mater. Res. 12 (1997) 1315–1326.
[2] T. Watanabe, K. Fujiwara, Nucleation and growth of oxide nanoparticles prepared by induction thermal plasmas, Chem. Eng. Commun. 191 (2004) 1343–1361.
[3] Y. Yao, T. Watanabe, T. Yano, T. Iseda, O. Sakamoto, M. Iwamoto, S. Inoue, An innovative energy-saving in-flight melting technology and its application in glass production, Sci. Technol. Adv. Mater. 9 (2008) 025013.
[4] T. Yoshida, K. Akashi, Particle heating in a radio-frequency plasma torch, J. Appl. Phys. 48 (1977) 2252–2260.
[5] M.I. Boulos, Heating of powders in the fire ball of an induction plasma, IEEE Trans. Plasma Sci. PS-6 (1978) 93–106.
[6] P. Proulx, J. Mostaghimi, M.I. Boulos, Plasma–particle interaction effects in induction plasma modeling under dense loading conditions, Int. J. Heat Mass Transfer 28 (1985) 1327–1335.
[7] J. Mostaghimi, M.I. Boulos, Two-dimensional electromagnetic field effects in induction plasma modeling, Plasma Chem. Plasma Process. 9 (1989) 25–44.
[8] J. Mostaghimi, K.C. Paul, T. Sakuta, Transient response of the radio frequency inductively coupled plasma to a sudden change in power, J. Appl. Phys. 83 (1998) 1898–1908.
[9] S.V. Patankar, Numerical Fluid Flow and Heat Transfer, Hemisphere, New York, 1980.
[10] Y. Tanaka, K.C. Paul, T. Sakuta, Thermodynamic and transport properties of N_2/O_2 mixtures at different admixture ratio, Trans. IEE Jpn. 120-B (2000) 24–30.
[11] X. Chen, E. Pfender, Effects of Knudsen number on heat transfer to a particle immersed into a thermal plasma, Plasma Chem. Plasma Process. 3 (1983) 97–113.
[12] Y.C. Lee, Y.P. Chyou, E. Pfender, Particle dynamics and particle heat and mass transfer in thermal plasmas. Part II. Particle heat and mass transfer in thermal plasmas, Plasma Chem. Plasma Process. 5 (1985) 391–414.
[13] C.T. Crowe, M.P. Sharma, D.E. Stock, The particle-source-in cell (PSI-CELL) model for gas-droplet flows, J. Fluid Eng. 99 (1977) 325–332.
[14] R. Ye, P. Proulx, M.I. Boulos, Particle turbulent dispersion and loading effects in an inductively coupled radio frequency plasma, J. Phys. D: Appl. Phys. 33 (2000) 2154–2162.